Shape of Asteroid 4769 Castalia (1989 PB) from Inversion of Radar Images

R. Scott Hudson* and Steven J. Ostro

The inversion of previously reported, delay-Doppler images of Castalia yields a 167-parameter, three-dimensional shape model that is bifurcated into two distinct, irregular, kilometer-sized lobes. The crevice that separates the lobes has an average depth of between 100 and 150 meters and is oriented roughly perpendicular to the asteroid's longest dimension. The constrained least-squares reconstruction method introduced here can be used to determine the shape, spin vector, and radar-scattering properties of any asteroid or comet for which delay-Doppler images provide sufficient signal-to-noise ratio, orientational coverage, and spatial resolution.

Radar observations can resolve Earth-crossing asteroids (ECAs) by measuring the distribution of echo power in time delay (range) and Doppler frequency: Planes normal to the line of sight cut the target into range cells, and for a rigid target, planes parallel to both the line of sight and the target's apparent spin vector (*1*) cut the target into Doppler-frequency cells (*2*). Hence, a delay-Doppler image can be visualized as the projection of the target's radar brightness onto a plane that contains the radar and is normal to the constant-delay, constant-Doppler lines. Each of those lines can intersect two or more noncontiguous points on the target; therefore, parts of the image can represent a many-to-one mapping, that is, can be "north/south ambiguous." Moreover, the length equivalent of frequency in radar images is a function of the target's apparent spin vector, which may be poorly known. The accurate interpretation of ECA radar images is consequently nontrivial and usually requires multiple images that sample diverse orientations of the target.

Radar observations (*3*) of 4769 Castalia (formerly 1989 PB) yielded useful resolution and definition of this ECA's shape: A 2.5-hour sequence of 64 images resolved the echo into a few dozen cells and revealed a bimodal distribution of echo power. Visual inspection and analysis of the echoes' frame-to-frame bandwidth variation indicated that Castalia is bifurcated into two kilometer-sized lobes apparently in contact with each other (*3*). In this report, we describe an estimation of Castalia's three-dimensional shape from the delay-Doppler images.

Each of the 64 images in our data set (*3*) is the result of a 29-s integration and consists of an estimate of radar cross section σ as a function of time delay τ and Doppler frequency ν. The length equivalent of the 2-μs interval between time samples is 300 m. The length equivalent of the frequency-sampling interval, where $\Delta\nu = 0.95$ Hz, is

$$\Delta\chi = \Delta\nu P\lambda/4\pi \cos\delta \quad (1)$$

where P is the apparent rotation period, λ is the wavelength (0.126 m), and δ is the subradar latitude (measured from the asteroid's equatorial plane to the radar line of sight). For the estimated period, 4.07 ± 0.02 hours (*3*), the 64-frame sequence covers 220° of rotation phase ψ; each image spans $\Delta\psi = 0.7°$. Because the asteroid's position on the sky changed by less than 1° during the entire imaging sequence, the contribution of that angular motion to the apparent rotation is negligible. We therefore assume that δ was constant throughout the sequence. Our shape reconstruction treated both δ and P as free parameters.

We used two shape models: a "one-component" model and a "two-component" model. The one-component model has a surface S defined by

$$S = \{\mathbf{r}|\mathbf{r} = r(\theta,\phi) [\sin\theta\cdot\cos\phi,\ \sin\theta\cdot\sin\phi,\ \cos\theta]\} \quad (2)$$

for $0 \le \theta \le \pi$ and $0 \le \phi < 2\pi$, where

$$r(\theta,\phi) = \sum_{l=0}^{L}\{a_{l0}P_l^0(\cos\theta) + \sum_{m=1}^{l}[a_{lm}\cos(m\phi) + b_{lm}\sin(m\phi)]P_l^m(\cos\theta)\} \quad (3)$$

is a spherical harmonic series having $(L + 1)^2$ "shape parameters" a_{lm}, b_{lm} (*4*). The surface of a two-component model is the union of the surfaces of two one-component models: $S = S_1 \cup S_2$, where $S_i = \{\mathbf{r}|\mathbf{r} = \mathbf{r}_i - \mathbf{r}_{0i}\}$ and $\mathbf{r}_i = r_i(\theta, \phi)[\sin\theta\cdot\cos\phi,\ \sin\theta\cdot\sin\phi,\ \cos\theta]$ for $i = 1, 2$. The radius functions r_1 (θ, ϕ) and $r_2(\theta, \phi)$ have their own spherical harmonic series, and $\mathbf{r}_{01}$ and $\mathbf{r}_{02}$ are the corresponding centers of the individual components.

We modeled the delay-Doppler data set as

$$\sigma_m(\tau,\nu;\psi) = \int\int I(\mathbf{r})h_\tau[\tau - \tau(\mathbf{r})]h_\nu[\nu - \nu(\mathbf{r})]\sigma_0(\mathbf{r})dS \quad (4)$$

Here $I(\mathbf{r})$ is unity if the point $\mathbf{r}$ is illuminated by the radar and zero otherwise, and h_τ and h_ν are the time and frequency impulse-response functions, respectively. The angular scattering law $\sigma_0(\mathbf{r})$, defined so $\sigma_0(\mathbf{r})dS$ is the radar cross section of a surface element dS at $\mathbf{r}$, is assumed to have the form

$$\sigma_0(\mathbf{r}) = \rho\cos^n i(\mathbf{r}) \quad (5)$$

where $i(\mathbf{r})$ is the angle of incidence, n measures the specularity of the surface, and ρ describes the radar brightness of the surface at normal incidence ($i = 0$). In addition we used 64 factors to permit the recalibration of each frame's brightness scale, which had relied on an empirical function describing the sensitivity of the Arecibo telescope; 64 delay-registration parameters to compensate for small, random, frame-to-frame shifts in the sampling time base; and a frequency offset to correct the a priori Doppler ephemeris.

The accuracy of any shape model derived from the Castalia data is limited by the fact that only one subradar latitude is sampled. If our view were too close to equatorial ($\delta \sim 0°$), the reconstruction would be north/south ambiguous. However, if $|\delta|$ were at least a few tens of degrees (as appears to be the case here), then the rotational phase coverage would provide sufficient geometric leverage to overcome north/south ambiguities (*5*), but the polar region opposite the radar-facing pole would have been unseen and hence poorly constrained. More generally, the data might support relatively high-resolution (large L) reconstruction of some regions of the surface (where the backscattering is strong or which contribute to many frames) but not others. We used the highest resolution (largest L) model that we felt was both computationally practical and adequate to ensure reliable reconstruction of well-imaged regions and then used penalty functions, described below, to suppress surface features that do not seem to be required by the observations. We settled on $L = 12$, or 169 shape parameters, for the one-component model and $L = 8$, or $2(8 + 1)^2 + 5 = 167$ shape parameters, for the two-component model (*6*). The total number of free parameters in the one- and two-component models were 300 and 298, respectively.

The reconstruction process minimized an objective function $\Phi(\mathbf{p})$ with the use of

R. S. Hudson, School of Electrical Engineering and Computer Science, Washington State University, Pullman, WA 99164–2752, USA.
S. J. Ostro, Jet Propulsion Laboratory, California Institute of Technology, Pasadena, CA 91109–8099, USA.
*To whom correspondence should be addressed.

Powell's method (7) to estimate the free parameters **p**. We took

$$\Phi(\mathbf{p}) = \chi^2(\mathbf{p}) + 10^{\beta_A}A(\mathbf{p}) + 10^{\beta_B}(\mathbf{p}) + 10^{\beta_C}C(\mathbf{p}) + 10^{\beta_D}D(\mathbf{p}) \quad (6)$$

where

$$\chi^2(\mathbf{p}) = \sum_{\tau\nu\psi}[\sigma_m(\tau,\nu;\psi) - \sigma(\tau,\nu;\psi)]^2/s^2_{\tau\nu\psi} \quad (7)$$

describes the goodness of fit between observed and modeled data. The variance $s^2_{\tau\nu\psi}$ of pixel $\tau\nu\psi$ includes contributions from receiver noise and echo self noise.

The "penalty functions" $A(\mathbf{p})$, $B(\mathbf{p})$, $C(\mathbf{p})$, and $D(\mathbf{p})$ are defined as follows: $A(\mathbf{p})$ is the square of the distance between the model's centroid and its spin axis, and $B(\mathbf{p})$ is the square of the sine of the angle γ between the spin axis and the model's principle axis of greatest moment of inertia. Making β_A and β_B large forces $A(\mathbf{p})$ and $B(\mathbf{p})$ to be small, producing a dynamically plausible model under the assumptions of uniform density and principle-axis rotation (8). The $C(\mathbf{p})$ function is a concavity penalty given by $C(\mathbf{p}) = \int\int U[k_m(\mathbf{r})]k_m^2(\mathbf{r})dS$, where U is the unit step function and $k_m(\mathbf{r})$ is the maximum surface curvature (9) at point **r**. Because $k_m(\mathbf{r}) > 0$ at a concavity, the integral is zero for a convex model, exceeds zero if any concavities exist, and increases as concavities become more prominent. The $D(\mathbf{p})$ function, a proximity penalty applicable only to two-component models, is the reciprocal of the distance between the components' centroids. Increasing β_C suppresses concavities, and increasing β_D forces the two components apart.

We obtained approximate values for the nonshape parameters from a biaxial ellipsoid fit to the data, used them to initialize the one-component model, and then sought a least-squares solution for the full parameter vector. The penalty factors β_A and β_B were set large enough to keep γ from exceeding a few degrees and to keep the centroid within a few tens of meters of the spin axis, and the concavity penalty factor β_C was set low enough to avoid any noticeable effect on the fits. This process yielded frame-to-frame calibration corrections on the order of 10% and delay registration corrections on the order of 0.5 μs, in each case consistent with a priori expectations about the performance of the Arecibo radar system (10). As an example of the model's sensitivity to a nonshape parameter, Fig. 1A shows values of postfit χ^2 versus values of the subradar latitude $|\delta|$ at 5° intervals.

The one-component estimations yielded distinctly nonellipsoidal shapes with a variety of concavities, notably a crevice, or waist, that encircles the middle of the body and is roughly perpendicular to the body's longest dimension. The value of χ^2 and the model's shape depend on the concavity penalty factor β_C (Figs. 1B and 2A), that is, on how strongly concavities are penalized. The penalizing of concavities by increasing β_C to 5 almost eliminates the waist but causes a severe increase in χ^2. We conclude that the waist is required to fit the data; Castalia is distinctly bifurcated into two lobes. We take the $\beta_C = 4$, one-component model to represent a lower bound on the asteroid's bifurcation.

To place an upper bound on the severity of the bifurcation, we used a two-component model and studied the dependence of shape and χ^2 on the proximity penalty factor β_D. The two-component parameter set and the penalty factors (β_A, β_B, β_C) were initialized with values from the $\beta_C = 4$, one-component model. However, here the concavity penalty function $C(p)$ was defined as the sum of integrals for each component, so it received no contribution from the waist, whose evolution was then independent of β_C (11). The χ^2 values and the shape depend on β_D (Figs. 1C and 2B), that is, on how strongly the component centroids are forced apart. At $\beta_D = 6$ the components are barely in contact, but χ^2 has increased dramatically. Substantial contact between the components is required to explain the data, and we take the $\beta_D = 5.4$, two-component model to represent an upper bound on the severity of Castalia's bifurcation.

We adopt the $\beta_D = 4$, two-component model (Fig. 3) as a nominal working model of the asteroid. The root-reduced chi-square

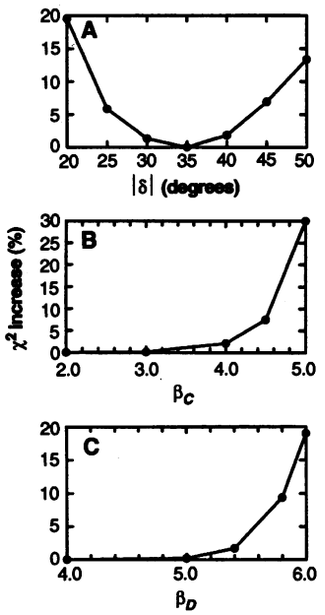

Fig. 1. (**A**) Percentage increase of χ^2 over its minimum value as a function of sub-radar latitude $|\delta|$ for estimations from the one-component model. The least-squares estimate, 35°, defines the locus of possible pole directions as a cone with axis parallel to the radar line of sight (right ascension = 0.30 hour, declination = 25.4°) and interior half angle 55° (16). Shape models for $|\delta|$ of 30° and 40° look similar to that for $|\delta|$ of 35°, whereas the models for 25° and 45° are noticeably smaller and larger, respectively. The inverse correlation between size and $|\delta|$ stems from Eq. 1, and the increase in χ^2 away from 35° reflects the pressure that the echoes' delay dispersion exerts on the estimation of the model's size. Based on our understanding of these results and numerous simulations, we assign an intentionally conservative standard error of ±10° to our estimate of $|\delta|$. (**B**) Percentage increase of χ^2 over its minimum value as a function of the concavity penalty factor β_C for estimations with the one-component model. (**C**) Percentage increase of χ^2 over its minimum value as a function of the proximity penalty factor β_D for estimations with the two-component model.

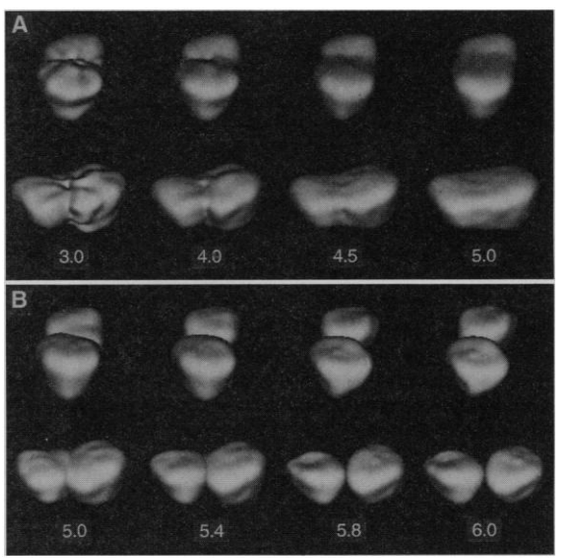

Fig. 2. (**A**) Plane-of-sky views of one-component models corresponding to $\beta_C = 3.0$, 4.0, 4.5, and 5.0. Views are at $\delta = 35°$ and rotation phases of $\psi \sim 53°$ (top row) and $\psi \sim 157°$ (bottom row), corresponding to frames 16 and 45, respectively, in figure 3 of (3). Models are rendered with a Lambertian ($n = 2$) scattering law. Values for χ^2 are essentially insensitive to $\beta_C \leq 3$, have increased by 2% at $\beta_C = 4$, and rise steeply thereafter. Much bumpiness is smoothed out as we raise β_C from 3 to 4, but the waist remains intact. We take the $\beta_C = 4$ model to represent a lower bound on Castalia's bifurcation. (**B**) Plane-of-sky views of two-component models corresponding to $\beta_D = 5.0$, 5.4, 5.8, and 6.0. Orientations and scattering law are the same as in (A). Values for χ^2 are essentially insensitive to $\beta_D \leq 5$, have increased by 2% at $\beta_D = 5.4$, and rise steeply thereafter. We take the $\beta_D = 5.4$ model to represent an upper bound on Castalia's bifurcation.

goodness-of-fit statistic, RRC = $[\chi^2/(N_d - N_p)]^{1/2}$, with N_d = 5824, the number of observed data, and N_p = 298, the number of free parameters, calculated over 2 by 2 km frames, is 1.5. This value of RRC might be interpreted to mean that the modeling is incomplete (for example, L may be too small) or inaccurate (for example, the assumed scattering law may be simplistic). However, the formal probabilistic interpretation of this statistic in linear least-squares estimation is not applicable here, primarily because of the extreme nonlinearity of the mathematical model and also because of the difficulty of quantifying the effective increase in the number of degrees of freedom that is caused by use of the penalty functions (*12*).

Nonetheless, we were concerned that our assumption of a uniform scattering law (Eq. 5) may have been overly restrictive. To test for the presence of variations in reflectivity ρ and specularity n, we explored one-component models that allowed both parameters to be functions of surface location, by expanding each in its own $L = 8$ spherical harmonic series. The estimation, which involved 160 new parameters, did not reduce RRC and hence fails to offer compelling evidence for heterogeneity in the radar properties of Castalia's surface. Large-scale (>100-m) variations in near-surface bulk density or roughness therefore seem unlikely (*13*).

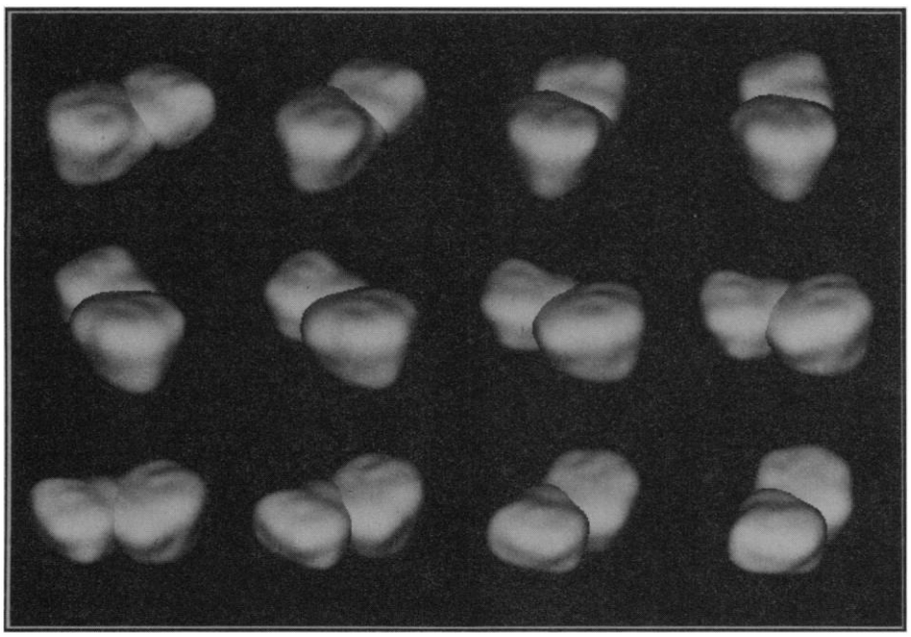

Fig. 3. Plane-of-sky views of the nominal model of Castalia at subradar latitude $\delta = 35°$ and rotation phases $\psi = 0°$ to 220° in steps of 20°. Lobe alpha (see Fig. 4) is between the viewer and lobe beta at $\psi = 60°$. The Lambertian scattering law used for this rendering and in Fig. 2 is somewhat less specular than the radar scattering law estimated in our reconstruction and much more specular than optical scattering laws thought to characterize asteroids.

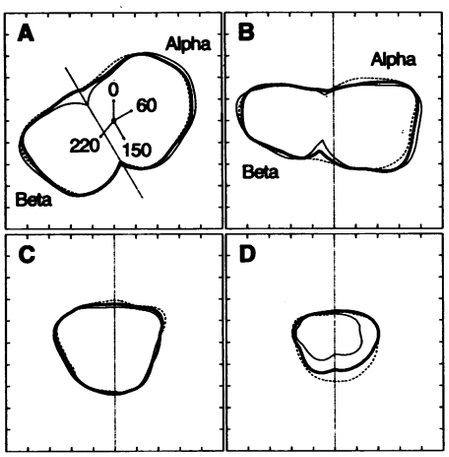

Fig. 4. Perspectives showing projections of the nominal Castalia model (thick solid curve), the lower bound model (dashed curve), and the upper bound model (thin solid curve). (**A**) Pole-on view of model silhouettes. The spin axis is denoted by the dot in lobe alpha. Arrows radiating from that dot point toward the radar at rotational phases $\psi = 0°$, 60°, 150°, and 220°; the radar data $\sigma(\tau,\nu;\psi)$ cover phases from 0° to 220°. (**B**) "Broadside" view from within the equatorial plane at $\psi = 150°$. (**C**) "End-on" views from within the equatorial plane at $\psi = 60°$. (**D**) Cross sections corresponding to the dotted-line slice through the pole-on view. The dotted vertical lines in (B), (C), and (D) represent the spin axis. Each quadrant is a 2 by 2 km square, and the tick marks are at 0.2-km intervals. The curve defined by the intersection of the two lobes in the nominal model is nonplanar. The root-mean-square deviation of that curve from its best-fit plane is 0.16 km. That plane lies 0.17 km from the nominal model's center of mass along a line that points toward $(\psi,\delta) = (241°,8°)$.

Our reconstruction shows Castalia to be a strongly bifurcated body whose convex hull has maximum dimensions of 0.7 by 1.0 by 1.6 km (Figs. 3 and 4). The asteroid's prominent waist has a typical depth between 100 and 150 m with respect to the object's convex hull. The depth and sharpness of the waist support the hypothesis (*3*) that at one time the lobes were separate and that the current "contact-binary" configuration resulted from a relatively gentle collision.

Our Castalia model is distinctly nonconvex and nonellipsoidal. Its volume (0.68 km^3) is 10% less than that of its convex hull, and its root-mean-square radial deviation from that hull (averaged over all θ,ϕ and normalized to the model's mean radius of 0.50 km) is Δr_{hull} = 10%. The model's deviation from its best triaxial-ellipsoidal approximation, Δr_{ell} = 14%, exceeds the corresponding value of 11% for the main belt asteroid 951 Gaspra (*14*). That asteroid deviates more from an ellipsoid than Phobos, Deimos, any other planetary satellite observed by spacecraft, or any asteroid for which stellar occultation limb profiles are available (*15*). Therefore Castalia, the smallest planetary object imaged so far, is also the most irregularly shaped. The individual lobes, labeled alpha and beta in Fig. 4, have mean radii of 0.46 and 0.40 km and Δr_{ell} of 11% and 12%, respectively.

The only fundamental limitations on the resolution of a shape reconstruction from radar images are the delay-Doppler resolution, orientational coverage, and signal-to-noise ratio of those images. The Arecibo and Goldstone radars can now achieve resolution an order of magnitude finer than that of the Castalia data. By 1995, completion of instrumentation upgrades now underway should allow the useful imaging and reconstruction of several of the currently known ECAs per year.

REFERENCES AND NOTES

1. The apparent spin vector ω at any time t is the sum of the intrinsic (sidereal) spin vector ω_s and the contribution $\omega_o = (de/dt) \times e$ arising from the changing direction of the target-to-radar unit vector e.
2. S. Hudson, *Remote Sensing Rev.* **8**, 195 (1993).
3. S. J. Ostro *et al.*, *Science* **248**, 1523 (1990).
4. T. Duxbury [*Icarus* **78**, 119 (1989)] outlined merits and drawbacks of the use of spherical harmonics to model irregularly shaped solar system objects. He fit a one-component model with $L = 6$ (that is, 49 shape parameters) to spacecraft images of Phobos.
5. If $\delta \neq 0$, every point on the surface executes a unique delay-Doppler trajectory as the target rotates.
6. Five parameters are needed to describe the locations of the components' centers relative to each other and to the spin vector.
7. W. H. Press, B. P. Flannery, S. A. Teukolsky, W. T. Vetterling, *Numerical Recipes in C* (Cambridge Univ. Press, Cambridge, 1988).
8. Because parts of the asteroid are not well constrained by the observations, we cannot test hypotheses that involve the object's internal density distribution or rotational stability. Our assumptions of uniform density and principal-axis rotation en-

sure the plausible extrapolation of the reconstructed surface into unconstrained regions.
9. D. J. Struik, *Lectures on Classical Differential Geometry* (Dover, New York, ed. 2, 1988).
10. Estimates of nonshape parameters include an independent value for the rotation period (P = 4.07 ± 0.03 hours) and refined values for the time delay τ and 2380-MHz Doppler frequency ν of hypothetical echoes from Castalia's center of mass. These values were received at the center of curvature of the Arecibo telescope's main reflector, at the epoch 22 August 1989 06:45:00 UTC: τ = 37,453,066.9 ± 0.3 μs and ν = 173,116.5 ± 0.1 Hz.
11. The Castalia data apparently require a waist with severe surface curvature. The rippled appearance of the low-β_C, one-component models in Fig. 2A is an artifact, called Gibbs' phenomenon, of trying to use a truncated series to represent a sharply curving, nearly discontinuous function. The two-component model avoids this drawback.
12. Removing the "dynamical" penalty functions $A(\mathbf{p})$ and $B(\mathbf{p})$ and allowing the nominal model to reconverge decreased χ^2 by less than 0.1%.
13. For the nominal model, estimates of the scattering-law exponent and reflectivity (see Eq. 5) are n = 2.8 ± 0.3 and ρ = 0.30 ± 0.03, where the uncertainties encompass values for the upper and lower bound models. The most commonly used measure of a radar target's reflectivity is the radar albedo $\hat{\sigma} = \sigma/A_p$, which is the target's radar cross section divided by its projected area. Castalia's model albedo, averaged over all 64 frames, is 0.12 ± 0.01. A sphere with Castalia's values for ρ and n would have a radar albedo $\hat{\sigma} = 2\rho/(n + 1) = 0.16 \pm 0.01$; this "equivalent spherical albedo" may permit more useful comparisons with other radar targets.
14. M. J. S. Belton *et al.*, *Science* **257**, 1647 (1992).
15. P. C. Thomas, *Icarus* **77**, 248 (1989).
16. For a single-δ observation, if δ is replaced by −δ and the model is replaced by its mirror image through the equatorial plane, then $\sigma_m(\tau,\nu;\psi)$ is unchanged. The spin vector's sign (that is, the sense of rotation) and its azimuthal coordinate could have been constrained if other radar-target directions had been sampled.
17. This research was conducted at Washington State University and the Jet Propulsion Laboratory, California Institute of Technology, under contract with the National Aeronautics and Space Administration.

30 September 1993; accepted 6 January 1994

The Cosmological Kibble Mechanism in the Laboratory: String Formation in Liquid Crystals

Mark J. Bowick,* L. Chandar, E. A. Schiff, Ajit M. Srivastava

The production of strings (disclination lines and loops) has been observed by means of the Kibble mechanism of domain (bubble) formation in the isotropic-nematic phase transition of the uniaxial nematic liquid crystal 4-cyano-4′-*n*-pentylbiphenyl. The number of strings formed per bubble is about 0.6. This value is in reasonable agreement with a numerical simulation of the experiment in which the Kibble mechanism is used for the order parameter space of a uniaxial nematic liquid crystal.

Symmetry-breaking phase transitions in nature often spawn topological defects. An example of such defects from condensed matter physics is vortices produced when helium is cooled through its superfluid phase transition. An important proposal from cosmology is that the observed structure of the universe contains relics of topological defects formed as the early universe cooled. The important question of the density of defects was first treated theoretically by Kibble (*1*) using a model in which the phase transition proceeds by the formation of uncorrelated domains that subsequently coalesce, leaving behind defects. A domain is a uniform region of the ordered, or low-temperature, phase. Kibble assumed that the order varied randomly from one domain to the next and smoothly in between, and so proposed a straightforward statistical procedure for calculating the probability of string formation.

Although the Kibble mechanism was proposed for cosmic domains and strings, it should also describe the formation of strings or line defects in laboratory systems. Some time ago, Zurek (*2*) suggested the examination of vortex formation in liquid helium. The first experimental success, however, came in research by Chuang and co-workers (*3, 4*). Working with nematic liquid crystals, these researchers were able to observe the evolution of line defects. In the present work, we report an experimental verification of a crucial aspect of the Kibble mechanism: String formation can be predicted statistically from domain coalescence. Experiments have also been reported recently on vortex line creation in liquid ^{4}He (*5*).

Nematic liquid crystals (NLCs) consist of rod-like molecules; the rods are randomly oriented in the isotropic, high-temperature phase but show long-range alignment in the nematic, orientationally ordered phase (*6*). To quantitatively distinguish the ordered and disordered phases, an order parameter is typically introduced. For NLCs, this parameter may be taken to be the mean orientation of rods. This value is zero in the isotropic phase and nonzero in the nematic phase. Orientational order in the nematic phase is described by a unit three vector $\mathbf{n}$ without sign, because there is no preferred polarity to the constituent rods ($\mathbf{n} \equiv \mathbf{n}$). Thus, the space of possible nematic ground states is the two-sphere S^2, with opposite points of the sphere regarded as the same (*7*). This space is rich in topological defects (*6–11*). It has point-like defects (monopoles), line defects (disclinations or strings), and three-dimensional defects (texture).

Before describing the present work with NLCs, we illustrate the Kibble mechanism using string formation for the simpler case of two spatial dimensions (planar spins) (*8*). The order parameter in some small spatial region is a unit vector with orientation θ varying between 0 and 2π (the ground-state manifold is a circle S^1). If we follow θ along a closed path, we can determine the total angle $\Delta\theta$ by which θ winds; of course $\Delta\theta$ must be some integer multiple of 2π. When $\Delta\theta$ is nonzero, a defect must be present inside the path (see Fig. 1A).

Consider now the situation when three randomly oriented domains meet at a point (Fig. 1B). We can then calculate the winding angle $\Delta\theta$ using a closed path that circulates in some specified direction around the intersection point; the dashed line in the figure illustrates such a path. If $\Delta\theta = +2\pi$, one type of elementary string is formed when the three domains coalesce.

The probability of string occurrence is

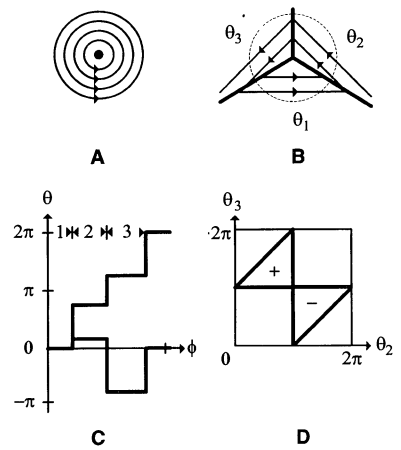

Fig. 1. A series of four diagrams illustrating the Kibble mechanism for planar spins. (**A**) The concentric circles indicate field lines of the order parameter and require an elementary topological defect at the origin. (**B**) Three domains with uniform order parameters θ_1, θ_2, and θ_3. The dashed circle indicates a loop around which a winding angle $\Delta\theta$ is calculated. (**C**) A graph illustrating the calculation of the winding angle for a path through three domains such as in (B). By definition, $\theta_1 = 0$. The jumps in θ between domains are minimized: This is the geodesic rule. Two different sets of order parameters are shown; the upper curve leads to defect formation ($\Delta\theta = +2\pi$), and the lower curve does not ($\Delta\theta = 0$). (**D**) The triangles labeled (+) and (−) indicate the combinations of θ_2 and θ_3 leading to $\Delta\theta = \pm 2\pi$ defects. One-fourth of all combinations lead to defect formation.

M. J. Bowick, L. Chandar, E. A. Schiff, Department of Physics, Syracuse University, Syracuse, NY 13244–1130, USA.
A. M. Srivastava, Institute for Theoretical Physics, University of California, Santa Barbara, CA 93106, USA.
*To whom correspondence should be addressed.